

Observation of a phase transition within the domain walls of the magnetic Weyl semimetal $\text{Co}_3\text{Sn}_2\text{S}_2$

Changmin Lee¹, Praveen Vir², Kaustuv Manna^{2,3}, Chandra Shekhar², J. E. Moore^{1,4}, M. A. Kastner^{5,6}, Claudia Felser², and Joseph Orenstein^{1,4}

¹ Materials Science Division, Lawrence Berkeley National Laboratory, Berkeley, California

² Max Planck Institute for Chemical Physics of Solids, Dresden, Germany

³ Department of Physics, Indian Institute of Technology Delhi, New Delhi, India

⁴ Department of Physics, University of California at Berkeley, Berkeley, California

⁵ Department of Physics, Stanford University, Palo Alto, California

⁶ Stanford Institute for Materials and Energy Science, SLAC National Accelerator Laboratory, Menlo Park, California

In magnetic Weyl semimetals, fluctuations of the local magnetization may generate gauge fields that couple to the chiral charge of emergent Weyl fermions. Recent theoretical studies have proposed that the temporal and spatial-dependent magnetization associated with propagating domain walls¹⁻⁴ (DWs) generates “pseudo” electric and magnetic fields that drive novel phenomena such as a current of “real” charge. Here we report a key step in testing these predictions: characterizing the propagation of DWs in the Weyl semimetal $\text{Co}_3\text{Sn}_2\text{S}_2$ using scanning magneto-optic Kerr microscopy. We observe an unexpected deep minimum in the temperature dependence of the DW mobility, μ , indicating a crossover between two regimes of propagation. The nonmonotonic $\mu(T)$ is evidence of a phase transition in the topology of the DW well below the Curie temperature, in which the magnetization texture changes from continuous rotation (elliptical wall) to a linear wall whose unidirectional magnetization passes through zero at the wall center.

Weyl semimetals are condensed matter systems in which nondegenerate bands cross at isolated points in momentum space⁵⁻⁷. Quasiparticles with momenta near each of the crossing points are emergent Weyl fermions, exhibiting linear dispersion and definite chirality. Because the band crossing points are monopoles of Berry curvature, it follows that either inversion or time-reversal symmetries must be broken to allow the WSM bandstructure. Although the inversion breaking class of WSMs was discovered first, the more elusive magnetic class is of great interest because spatial and temporal variations in magnetization, as exemplified by DW motion, generate emergent gauge fields that couple to both chiral and “real” charge density³.

The ferromagnetic shandite $\text{Co}_3\text{Sn}_2\text{S}_2$ has recently been identified as a magnetic Weyl semimetal that exhibits a giant anomalous Hall effect originating from the strong Berry curvature associated with its Weyl nodes⁸⁻¹⁰. The dispersion of Fermi arc surface states has been observed by photoemission¹¹ and scanning tunneling measurements¹² and their dependence on crystal surface termination is consistent with bandstructure calculations. The magnetism of $\text{Co}_3\text{Sn}_2\text{S}_2$ arises from Kagome layers of Co and manifests a strong easy axis anisotropy favoring magnetization perpendicular to the layers.

A persistent puzzle in studies of $\text{Co}_3\text{Sn}_2\text{S}_2$ is the observation by static and ac susceptibility¹³, Hall effect¹⁴, and muon spin rotation¹⁵, of an anomaly in the temperature dependence near 130 K, well below the Curie temperature of 175 K. Proposed explanations for these features include spin glass¹⁴ and non-collinear antiferromagnetic order coexisting with uniaxial ferromagnetism¹⁵. The scanning Kerr microscopy measurements of local domain wall dynamics described below provide

strong evidence that the anomalies reported previously derive from a phase transition that takes place within the domain walls.

A schematic of the experimental setup is shown in the upper half of Figure 1(a), which illustrates local probing of the magnetization using the polar Kerr effect. Scanning the sample under the laser focus yields a map (Fig. 1(b)) of the Kerr ellipticity, $\Phi(\mathbf{r})$, revealing domains of magnetization directed parallel and anti-parallel to the surface normal, which we take to be the z direction. Measuring the change in $\Phi(\mathbf{r})$ across a domain wall yields a measure of the zero-field magnetization, which is plotted as a function of temperature in the lower half of Fig. 1(a) (see Supplementary Information Section I for details). A coil surrounding the sample generates an oscillating magnetic field parallel to the easy axis, $H_z(t) = H\sin\omega t$, that tilts the energy landscape, inducing DW displacement in the direction that increases the volume of magnetization aligned parallel to $H_z(t)$. The oscillating displacement in turn generates a synchronous modulation, $\delta\Phi_{ac}(\mathbf{r})$, that peaks at the domain boundaries. Fig. 1(c) shows a map of $\delta\Phi_{ac}(\mathbf{r})$ normalized to the static Kerr ellipticity within a domain, Φ_{dc} , which shows peak contrast at the domain walls imaged in Fig. 1(b).

Figure 2 shows a series of maps that illustrate the temperature dependence of $\delta\Phi_{ac}(\mathbf{r})/\Phi_{dc}$ in the range from 120 K to the Curie temperature. Two features are immediately clear from the sequence of images. First, as the temperature is increased to 160 K, each domain boundary becomes increasingly convoluted, suggesting a progressive decrease in surface tension. A second, and perhaps more unexpected feature is the non-monotonic amplitude of $\delta\Phi_{ac}(\mathbf{r})/\Phi_{dc}$ as a function

of T ; this is especially apparent in the $T = 140$ K map, where the $\delta\Phi_{ac}(\mathbf{r})/\Phi_{dc}$ signal is significantly reduced and the DWs are nearly invisible.

Panels (a)-(d) of Figure 3 illustrate the local dynamics of a representative segment of a DW as determined from $(\delta\Phi_{ac}/\Phi_{dc})_{DW}$, which is the maximum value of $\delta\Phi_{ac}(\mathbf{r})/\Phi_{dc}$ measured on a scan the normal to a domain boundary (See Supplementary Information Section V for details on the spatial variation of DW mobility). Fig. 3(a) presents an overview of $(\delta\Phi_{ac}/\Phi_{dc})_{DW}$ in the $\omega - T$ plane using a color scale; Fig. 3(b) shows several line cuts through the plane at constant ω . A deep minimum in $(\delta\Phi_{ac}/\Phi_{dc})_{DW}$ near 140 K is evident in both plots.

The key advantage of scanned local probe over global ac susceptibility measurements is the ability to determine the displacement, Δx , of an individual domain wall. In the regime where the DW width, w , is smaller than the laser focal radius, σ , the displacement is obtained from $(\delta\Phi_{ac}/\Phi_{dc})_{DW} = \text{erf}(\Delta x/\sqrt{2}\sigma)$, where $(\delta\Phi_{ac}/\Phi_{dc})_{DW}$ is the ratio of $\delta\Phi_{ac}$ at the wall center to the step in Φ_{dc} across the DW. This relation is modified at temperatures above 160 K where w becomes comparable to σ (see Supplementary Information Sections II and III).

Fig. 3(c) shows the displacement of an individual wall segment as a function of H for several frequencies as determined from $(\delta\Phi_{ac}/\Phi_{dc})_{DW}$. The wall displacement displays a threshold, indicating collective pinning behavior; Δx is nearly zero for H below a frequency dependent field, H_{th} , and increases rapidly for $H > H_{th}$. In the next step of analysis, we conjecture that the dependence of Δx on ω and H reflects a relation between instantaneous velocity and field of the form, $dx/dt = \mu H_{th} f(H/H_{th})$, where μ is a parameter with dimension of domain mobility and

$f(H/H_{th})$ is a dimensionless scaling function. It follows from this ansatz that the product $\omega\Delta x/H_{th}$ depends only on the ratio H/H_{th} (see Supplementary Information Section IV). Fig. 3(d) shows that plotting $\omega\Delta x/H_{th}$ vs. H/H_{th} collapses the data set shown in Fig. 3(c) to a single curve, providing strong evidence for the picture of a field-dependent velocity.

The scaling plot allows us to test a simple version of threshold behavior, in which $dx/dt=0$ for $H < H_{th}$ and $dx/dt = \mu(H - H_{th})$ for $H > H_{th}$. In this case the scaling function is given by

$$F(\rho) \equiv \frac{\mu}{\rho} \int_1^\rho \frac{dy(y-1)}{\sqrt{1 - \left(\frac{y}{\rho}\right)^2}}, \quad (1)$$

where $\rho \equiv H/H_{th}$ (see Supplementary Section IV). As seen in Fig. 3(d) the collapsed data is in quite reasonable agreement with $F(\rho)$, although the transition to high mobility at $H = H_{th}$ is smooth, rather than singular. The best fit to the collapsed data determines μ , which is now interpreted as the differential mobility for $H > H_{th}$.

Fig. 3(e) shows the differential mobility, μ , as a function of T in the range from 110-165 K, obtained by performing the scaling procedure described above. The deep minimum in DW mobility at 145 K cannot be understood within the standard theory of DW dynamics, which assumes a Bloch wall topology where \mathbf{M} rotates with constant magnitude in the plane of the DW. Below the Walker breakdown velocity the Bloch DW mobility is given by $\mu_B = \gamma w/\alpha$, where α is the Gilbert parameter describing the damping rate of transverse magnetization fluctuations, γ is the gyromagnetic ratio, and w is the DW width¹⁶. While disorder could account for a monotonic decrease in mobility as T is lowered, it is very difficult to explain the subsequent increase of μ below ≈ 130 K.

Studies of the ac susceptibility, χ_ω , of insulating orthoferrite magnets performed in the early 1990's provide a clue as to the origin of the anomalous $\mu(T)$ in $\text{Co}_3\text{Sn}_2\text{S}_2$. These measurements revealed a minimum in $\chi_\omega(T)$ similar to the DW mobility minimum we observe in $\text{Co}_3\text{Sn}_2\text{S}_2$, although at temperatures much closer to T_c ¹⁷⁻¹⁹. The origin of this phenomenon was traced to the prediction by Bulaevskii and Ginzburg (BG)²⁰ that DWs undergo a phase transition at a temperature T_{BG} , below T_c , which was subsequently shown to be analogous to a transition from ϕ^4 to sine-Gordon solitons^{21,22}.

The origin of the BG phase transition is the crossover between the uniaxial anisotropy energy and the energy required to change $|\mathbf{M}|$, as parameterized by the longitudinal susceptibility, $\chi_{||}$. As $T \rightarrow T_c$, $\chi_{||}$ diverges, whereas the anisotropy coefficient varies smoothly. Therefore, in some range of temperature below T_c a linear wall, in which \mathbf{M} remains aligned along the easy axis and passes through zero at the DW center, has lower energy than the Bloch wall. Thus, a phase transition in DW texture (with increasing T) from circular or elliptic to linear wall is predicted, whose order parameter is the component of \mathbf{M} perpendicular to the easy axis (see illustrations in Figs. 3(f-h)).

The dynamics of wall motion are different for elliptical as opposed to linear domain walls. The motion of Bloch walls, as described by the Landau-Lifshitz-Gilbert (LLG) equation²³⁻²⁵, depends crucially on torque arising from the component of \mathbf{M} transverse to the easy axis, which is perpendicular to $H_z(t)$. By contrast, the torque on the linear DW is zero. To describe the DW mobility through the linear to elliptical transition, Garanin added a term to the LLG equation of the form $\dot{M}_z(t) = \gamma_L H_z(t)$, where γ_L describes relaxation of longitudinal fluctuations²². In this

theory the mobility of a linear DW is independent of the gyromagnetic ratio, and instead is given by $\mu_{LW} = (3/2)\gamma_L w$. The linear wall mobility decreases rapidly below T_c because w is equal to the decreasing magnetic correlation length²⁰. However, the onset of transverse magnetization, M_x , at the DW phase transition leads to an increase in mobility given by $\mu(T) \approx \mu_{LW}/(1 - M_x/M_z)$ for temperatures just below T_{BG} . The dashed line in Fig. 3(e) is a fit of the full expression derived by Garanin to the measured $\mu(T)$, showing that the BG transition can account for the non-monotonic DW mobility²² (see Supplementary Information Section VI).

We now turn to the T dependence of the static MOKE images, which provides further evidence for the existence of linear domain walls below T_c . We observed a set of striking domain nucleation phenomena by cooling samples to 100 K in an external field sufficient to prepare a single domain state, removing the field, and warming to the Curie temperature. At a nucleation temperature, $T_n \ll T_c$, domains appear abruptly out of the uniformly magnetized state. Figs. 4(a) and (b) shows the transition from a uniform to multi-domain state sampled at a temperature interval of 100 mK. Remarkably, the transition is even more abrupt; Fig. 4(c) shows that the magnetization flips from one fully saturated state to the other (i.e. from red to blue in the color code of Figs. 4(a) and 4(b)) when the sample temperature is raised by only 10 mK.

The sharpness of the transition provides an opportunity to test the mechanism of domain nucleation. In the usual picture, domains form as a result of thermal excitation over a barrier set by the domain wall energy. Because the nucleation rate is thermally activated, an implicit feature of this model is that T_n should increase logarithmically with the rate of heating (see Supplementary Information Section VII). However, measurements of T_n performed at several sample locations showed that T_n

is independent of heating rate, excluding thermal activation as mechanism. These results suggest strongly that T_n is, in fact, the temperature at which the barrier itself goes to zero. Below we show that, in contrast with Bloch walls, the barrier to formation of linear DWs goes to zero at a temperature well below T_c . Furthermore, we account for the dependence of T_n on an external field applied during the warming cycle.

We write the free energy density of magnetic texture as the sum of exchange, longitudinal susceptibility, and Zeeman energies^{19,26}:

$$F = M_s^2 \int dx \left[\rho_s \left(\frac{dm}{dx} \right)^2 + \frac{1}{4\chi_{\parallel}} (m^2 - 1)^2 + m \right], \quad (2)$$

where m is the z component of the magnetization normalized to M_s , the saturation value, ρ_s is the spin stiffness parameter, and χ_{\parallel} is the susceptibility for longitudinal fluctuations in M_z . Here we have assumed a demagnetization factor of unity (see Supplementary Information Section VIII). Notice that the anisotropy energy does not appear in F because of the assumption of a linear wall.

We assume that domain nucleation occurs via the generation of a DW pair with magnetization profile²⁶,

$$m(x, s, w) = 1 - \left[\tanh\left(\frac{x+s}{w}\right) + \tanh\left(\frac{-x+s}{w}\right) \right], \quad (3)$$

where s is pair separation. Substituting Eq. 6 into Eq. 5 yields $\Delta F(s)$, the change in free energy as a function of DW separation (see Supplementary Information Section VIII for details). In Fig. 4(d) we plot $\Delta F/M_s^2 w$ vs. s/w for values of χ_{\parallel} in the range from 0.4 to 1, showing that the barrier to domain wall nucleation vanishes for $\chi_{\parallel} \approx 0.6$. The vanishing of the nucleation barrier is a

unique property of a linear wall, as the barrier to Bloch or Neel wall formation is set by the anisotropy parameter, rather than $\chi_{||}(T)$.

The model described above can be extended to predict the shift in T_n if the sample is warmed in the presence of a small external H_z applied opposite to the direction of the metastable uniform magnetization,

$$\frac{dT_n}{dH_z} = \frac{1}{M_s \left[\frac{d}{dT} \ln\{\chi(T)\} \right]_{T=T_n}}, \quad (5)$$

(see Supplementary Information Section IX). A divergent $\chi_{||} \propto (T_c - T)^{-\gamma}$ with $\gamma = 1.24$ for the 3D Ising model and the saturation magnetization 880 Oe yields,

$$\frac{dT_n}{dH_z} \approx \frac{T_c - T_n}{\gamma M_s} \approx \frac{0.041 \text{ K}}{\text{Oe}}, \quad (6)$$

which is in reasonable agreement with the experimental value of 0.030 K/Oe as depicted in Fig. 4(e).

In summary, we have demonstrated a novel method of probing the previously unexplored dynamics of individual DWs in a magnetic Weyl semimetal, revealing wall motion when an applied ac magnetic field exceeds a threshold value. The observation of DW motion motivates future experiments to detect the charge current and other phenomena²⁷⁻³⁰ predicted to arise from the emergent gauge fields that accompany a propagating DW. Our measurements of the differential DW mobility across a wide range of frequency and temperature provide evidence for a phase transition within the DWs in which the magnetization profile changes from linear to elliptical with decreasing temperature. From the standpoint of topological band structure, the fact that the magnetization of linear walls vanishes at the wall center implies that time-reversal symmetry is

restored locally, either annihilating the Weyl nodes or transforming them to single Dirac point. Further understanding of DW dynamics in $\text{Co}_3\text{Sn}_2\text{S}_2$ and related Weyl semimetals requires consideration of the DW dynamics that result from this local topological phase transition.

Methods

Scanning MOKE microscopy

A linearly polarized 633 nm HeNe laser beam was focused at normal incidence onto a 1 μm spot on the sample surface with an objective lens (Olympus LMPFLN 50x, NA = 0.5). The reflected beam was then collected by a 50:50 non-polarizing beam splitter, which directs the beam to a quarter wave plate and a Wollaston prism for balanced photodetection of Kerr ellipticity. The sample position was raster scanned with xy piezoelectric scanners (Attocube ANPx101) and the focusing was fine-adjusted with a z piezoelectric scanner (Attocube ANPz102). An out-of-plane AC magnetic field was applied through a coil (Woodruff Scientific, 156 turns, inner diameter: 5mm, height: 1.5 mm) that surrounds the sample. A dc magnetic field was applied through the same coil for domain nucleation measurements.

Acknowledgement

We would like to thank Jeffrey Orenstein and Simon Woodruff for design of the magnetic coils used in the measurements, and Jonathan Denlinger for assistance in sample characterization. This work was primarily supported by the Quantum Materials program under the Director, Office of Science, Office of Basic Energy Sciences, Materials Sciences and Engineering Division, of the

U.S. Department of Energy, Contract No. DE-AC02-05CH11231. M.K. acknowledges support from the U.S. Department of Energy, Office of Science, Basic Energy Sciences, Materials Sciences and Engineering Division, under Contract DE-AC02-76SF00515. J.O. received support for optical measurements from the Gordon and Betty Moore Foundation's EPiQS Initiative through Grant GBMF4537 to J.O. at UC Berkeley. P.V., K.M., C.S., and C.F. acknowledge financial support from the European Research Council (ERC) Advanced Grant No. 742068 "TOP-MAT"; European Union's Horizon 2020 research and innovation program (Grant Nos. 824123 and 766566) and Deutsche Forschungsgemeinschaft (DFG) through SFB 1143. K. M. acknowledges the Max Planck Society for the funding support under Max Planck–India partner group project.

Author Contributions

C.L. performed the optical measurements. C.L. and J.O. analyzed the data and wrote the manuscript. P.V., K.M., C.S., and C.F. grew and characterized the crystals. J.O. and J.E.M. developed the theoretical models. All authors commented on the manuscript.

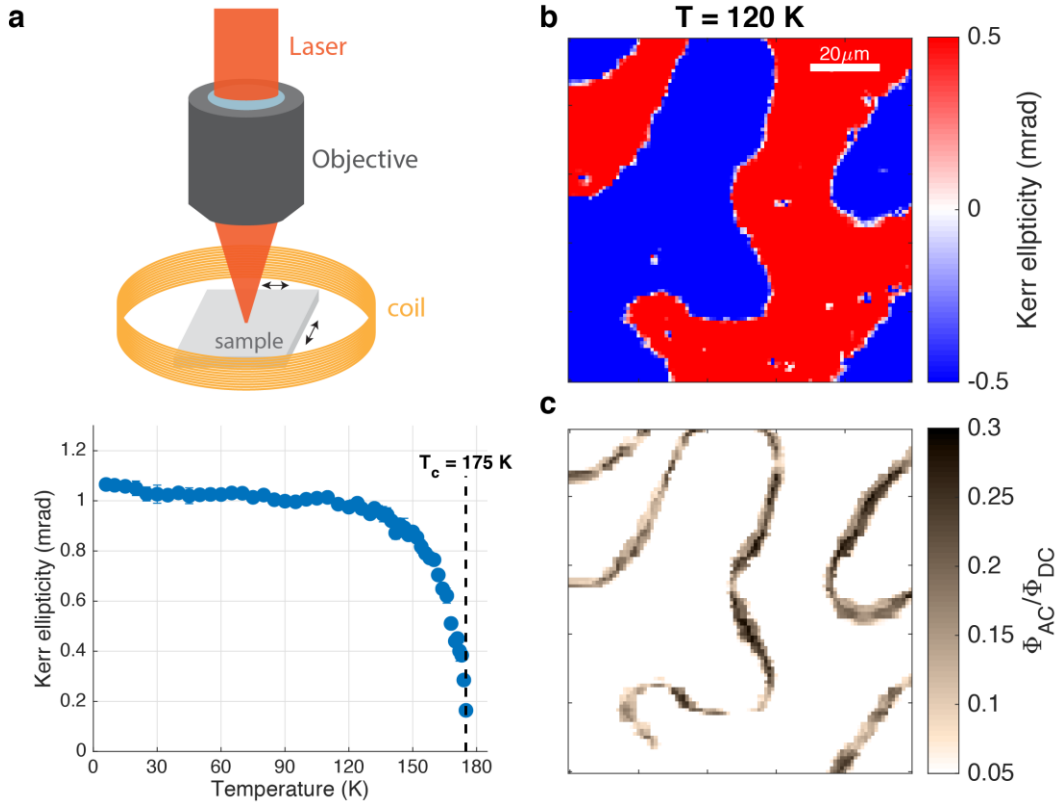


Figure 1 | Scanning Kerr microscopy. **a** (upper panel) Overview of ac MOKE microscopy setup. The sample is surrounded by a coil that generates an out-of-plane ac magnetic field. (lower panel) Temperature dependence of the change dc Kerr ellipticity across a domain wall. **b** Unmodulated Kerr ellipticity map taken at $T = 120$ K reveals stripe-like magnetic domains. **c** Modulated ($f = 1$ kHz) ac Kerr map measured over the same region of sample exhibits a strong signal at the domain boundaries. The signal is normalized by the dc Kerr ellipticity obtained at 120 K.

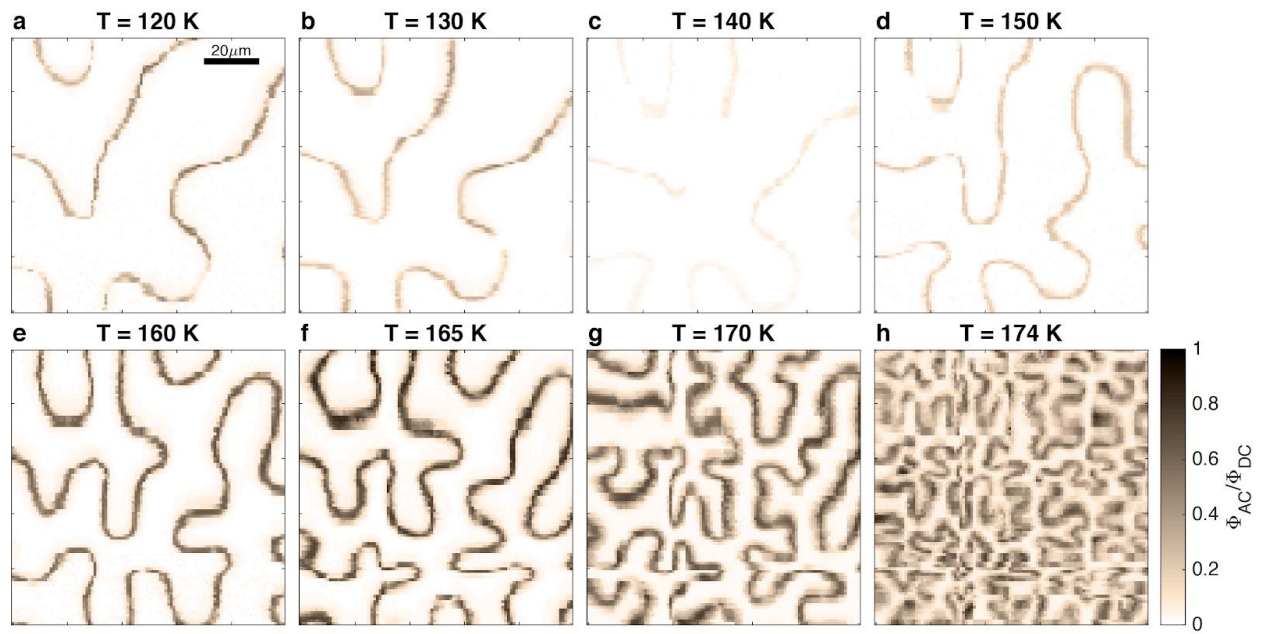


Figure 2 | AC Kerr ellipticity maps. a-h ac MOKE maps measured at temperatures ranging from 120 to 174 K. A 27 Oe ac magnetic field was applied at a frequency of 1kHz. The normalized ac Kerr ellipticity amplitude Φ_{AC}/Φ_{DC} is significantly reduced at 140 K.

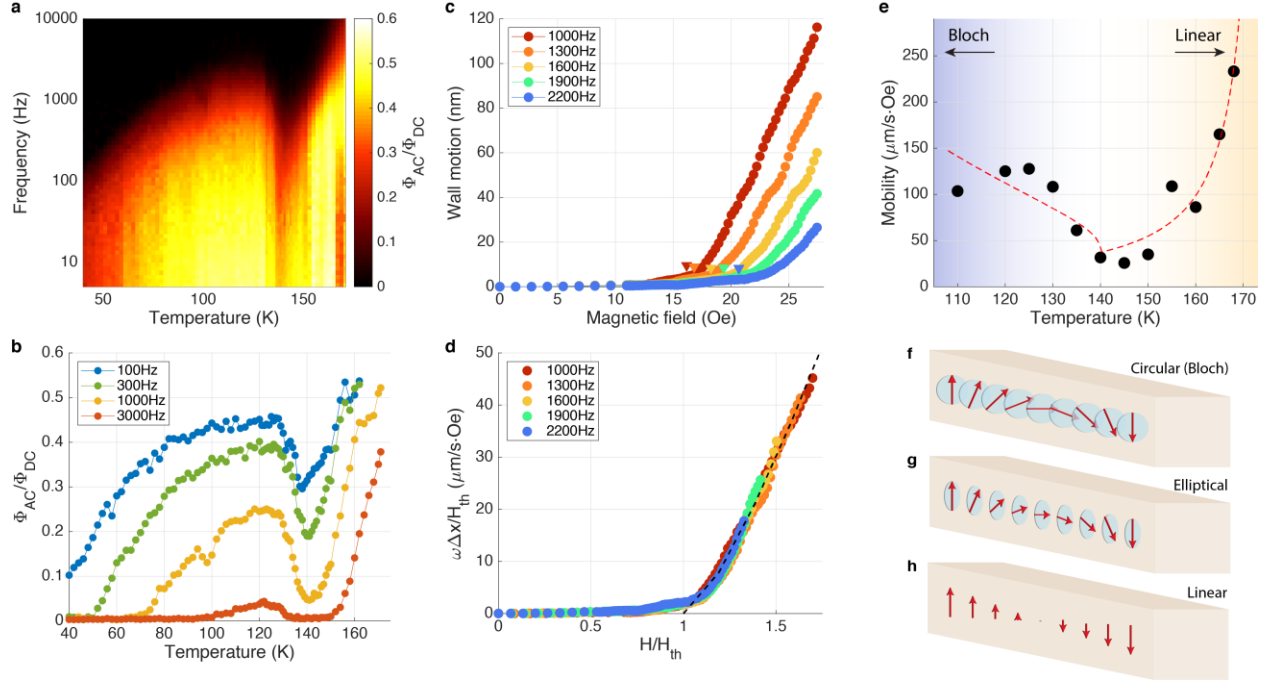


Figure 3 | DW mobility and linear wall phase transition. **a** Normalized ac Kerr response measured at a segment of a domain wall over a range of frequency (5 Hz – 10 kHz) and temperature (40 – 175 K). **b** Selected plots of the temperature dependence at constant frequency (horizontal cuts through the frequency-temperature map shown in **a**). **c** Measurements of the domain wall displacement plotted against ac magnetic field amplitude at $T = 130$ K. Threshold fields H_{th} are marked by inverted triangle symbols. **d** Scaling of the response illustrated by plotting $\omega \Delta x / H_{th}$ against H / H_{th} . The differential domain wall mobility above threshold is obtained from the slope at $H / H_{th} > 1$. **e** Domain wall mobility vs temperature. The non-monotonic temperature dependence of the mobility can be understood as a phase transition from an **f**, circular or **g**, elliptical wall to an **h**, linear wall in which the magnetization vanishes at the wall center.

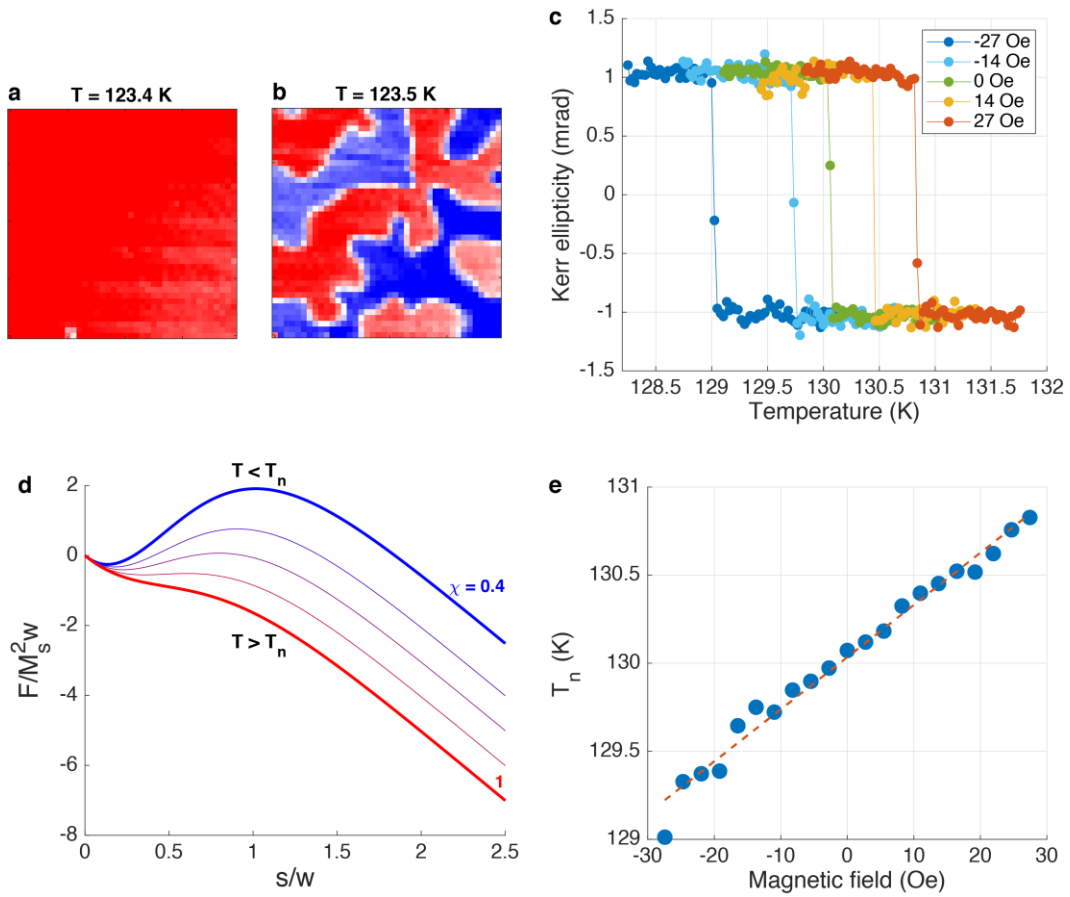


Figure 4 | Sudden domain nucleation of a field-cooled sample. a-b Maps illustrating the nucleation of a multi-domain state from a single domain that occurs upon warming by 100 mK. **c** Recording the MOKE signal vs. temperature from a single pixel within a blue domain shows that the transition to a multi-domain state takes place with a temperature increment less than 25 mK. A small out-of-plane magnetic field tunes the transition temperature. **d** A plot of $F/M_s^2 w$ for a linear domain wall as a function of w/s , for selected values of χ_{\parallel} . With increasing temperature the free energy barrier continuously decreases to zero, resulting in a sudden nucleation of magnetic domains. **e** Linear relationship between T_n and magnetic field as obtained from the data shown in **d**.

References

- 1 Liu, C.-X., Ye, P. & Qi, X.-L. Chiral gauge field and axial anomaly in a Weyl semimetal. *Physical Review B* **87**, doi:10.1103/PhysRevB.87.235306 (2013).
- 2 Grushin, A. G., Venderbos, J. W. F., Vishwanath, A. & Ilan, R. Inhomogeneous Weyl and Dirac Semimetals: Transport in Axial Magnetic Fields and Fermi Arc Surface States from Pseudo-Landau Levels. *Physical Review X* **6**, doi:10.1103/PhysRevX.6.041046 (2016).
- 3 Araki, Y. Magnetic Textures and Dynamics in Magnetic Weyl Semimetals. *Annalen der Physik* **532**, 1900287, doi:10.1002/andp.201900287 (2019).
- 4 Ilan, R., Grushin, A. G. & Pikulin, D. I. Pseudo-electromagnetic fields in 3D topological semimetals. *Nature Reviews Physics* **2**, 29-41, doi:10.1038/s42254-019-0121-8 (2019).
- 5 Wan, X., Turner, A. M., Vishwanath, A. & Savrasov, S. Y. Topological semimetal and Fermi-arc surface states in the electronic structure of pyrochlore iridates. *Physical Review B* **83**, doi:10.1103/PhysRevB.83.205101 (2011).
- 6 Burkov, A. A. & Balents, L. Weyl semimetal in a topological insulator multilayer. *Phys Rev Lett* **107**, 127205, doi:10.1103/PhysRevLett.107.127205 (2011).
- 7 Armitage, N. P., Mele, E. J. & Vishwanath, A. Weyl and Dirac semimetals in three-dimensional solids. *Reviews of Modern Physics* **90**, doi:10.1103/RevModPhys.90.015001 (2018).
- 8 Xu, Q. *et al.* Topological surface Fermi arcs in the magnetic Weyl semimetal Co₃Sn₂S₂. *Physical Review B* **97**, doi:10.1103/PhysRevB.97.235416 (2018).
- 9 Liu, E. *et al.* Giant anomalous Hall effect in a ferromagnetic Kagome-lattice semimetal. *Nat Phys* **14**, 1125-1131, doi:10.1038/s41567-018-0234-5 (2018).
- 10 Wang, Q. *et al.* Large intrinsic anomalous Hall effect in half-metallic ferromagnet Co₃Sn₂S₂ with magnetic Weyl fermions. *Nat Commun* **9**, 3681, doi:10.1038/s41467-018-06088-2 (2018).
- 11 Liu, D. F. *et al.* Magnetic Weyl semimetal phase in a Kagome crystal. *Science* **365**, 1282-1285, doi:10.1126/science.aav2873 (2019).

- 12 Morali, N. *et al.* Fermi-arc diversity on surface terminations of the magnetic Weyl semimetal Co₃Sn₂S₂. *Science* **365**, 1286-1291, doi:10.1126/science.aav2334 (2019).
- 13 Kassem, M. A., Tabata, Y., Waki, T. & Nakamura, H. Low-field anomalous magnetic phase in the kagome-lattice shandite Co₃Sn₂S₂. *Physical Review B* **96**, doi:10.1103/PhysRevB.96.014429 (2017).
- 14 Lachman, E. *et al.* Exchange biased anomalous Hall effect driven by frustration in a magnetic kagome lattice. *Nat Commun* **11**, 560, doi:10.1038/s41467-020-14326-9 (2020).
- 15 Guguchia, Z. *et al.* Tunable anomalous Hall conductivity through volume-wise magnetic competition in a topological kagome magnet. *Nat Commun* **11**, 559, doi:10.1038/s41467-020-14325-w (2020).
- 16 Schryer, N. L. & Walker, L. R. The motion of 180° domain walls in uniform dc magnetic fields. *Journal of Applied Physics* **45**, 5406-5421, doi:10.1063/1.1663252 (1974).
- 17 Kotzler, J., Garanin, D. A., Hartl, M. & Jahn, L. Evidence for critical fluctuations in Bloch walls near their disordering temperature. *Phys Rev Lett* **71**, 177-180, doi:10.1103/PhysRevLett.71.177 (1993).
- 18 Kötzler, J., Hartl, M. & Jahn, L. Signature of linear (Bulaevskii–Ginzburg) domain walls near T_c of Ba-hexaferrite. *Journal of Applied Physics* **73**, 6263-6265, doi:10.1063/1.352664 (1993).
- 19 Hartl-Malang, M., Kotzler, J. & Garanin, D. A. Domain-wall relaxation near the disorder transition of Bloch walls in Sr hexaferrite. *Phys Rev B Condens Matter* **51**, 8974-8983, doi:10.1103/physrevb.51.8974 (1995).
- 20 Bulaevskii, L. N. & Ginzburg, V. L. Temperature Dependence of the Shape of the Domain Wall in Ferromagnetics and Ferroelectrics. *Sov. Phys. JETP* **18** (1964).
- 21 Sarker, S., Trullinger, S. E. & Bishop, A. R. Solitary-wave solution for a complex one-dimensional field. *Physics Letters A* **59**, 255-258, doi:10.1016/0375-9601(76)90784-2 (1976).
- 22 Garanin, D. A. Dynamics of elliptic domain walls. *Physica A: Statistical Mechanics and its Applications* **178**, 467-492, doi:10.1016/0378-4371(91)90033-9 (1991).

- 23 Landau, L. & Lifshitz, E. On the theory of the dispersion of magnetic permeability in ferromagnetic bodies. 51-65, doi:10.1016/b978-0-08-036364-6.50008-9 (1992).
- 24 Gilbert, T. L. Classics in Magnetism A Phenomenological Theory of Damping in Ferromagnetic Materials. *IEEE Transactions on Magnetism* **40**, 3443-3449, doi:10.1109/tmag.2004.836740 (2004).
- 25 Lakshmanan, M. The fascinating world of the Landau-Lifshitz-Gilbert equation: an overview. *Philos Trans A Math Phys Eng Sci* **369**, 1280-1300, doi:10.1098/rsta.2010.0319 (2011).
- 26 Loxley, P. N. Rate of magnetization reversal due to nucleation of soliton-antisoliton pairs at point-like defects. *Physical Review B* **77**, doi:10.1103/PhysRevB.77.144424 (2008).
- 27 Hannukainen, J. D., Ferreiros, Y., Cortijo, A. & Bardarson, J. H. Axial anomaly generation by domain wall motion in Weyl semimetals. *Physical Review B* **102**, doi:10.1103/PhysRevB.102.241401 (2020).
- 28 Hannukainen, J. D., Cortijo, A., Bardarson, J. H. & Ferreiros, Y. Electric manipulation of domain walls in magnetic Weyl semimetals via the axial anomaly. arXiv:2012.12785 (2020).
- 29 Araki, Y., Yoshida, A. & Nomura, K. Universal charge and current on magnetic domain walls in Weyl semimetals. *Physical Review B* **94**, doi:10.1103/PhysRevB.94.115312 (2016).
- 30 Araki, Y., Yoshida, A. & Nomura, K. Localized charge in various configurations of magnetic domain wall in a Weyl semimetal. *Physical Review B* **98**, doi:10.1103/PhysRevB.98.045302 (2018).

Supplementary Information

“Observation of a phase transition within the domain walls of the magnetic Weyl semimetal $\text{Co}_3\text{Sn}_2\text{S}_2$ ”

I. DC Kerr ellipticity on traversing a domain wall

The unmodulated, dc Kerr ellipticity was measured as a function of position transverse to the domain walls. Typically, three consecutive scans through a wall were recorded to improve signal to noise ratio (Fig. S1(a)). The results were then fitted to an error function whose amplitude is proportional to the z component of the magnetization, M_z , within a domain. Φ_{dc} is therefore a measure of the equilibrium M_z in zero applied field.

The temperature dependence of Φ_{dc} is shown in Fig. S1(b), with two fits (red curves) that span the low temperature spin wave regime and the high temperature critical regime. In the high temperature regime, the best fit was obtained with Curie temperature $T_c = 175.2 \pm 0.2$ K and critical exponent $\beta = 0.33 \pm 0.03$, which is in good agreement with $\beta = 0.326$ predicted by the 3D Ising model.

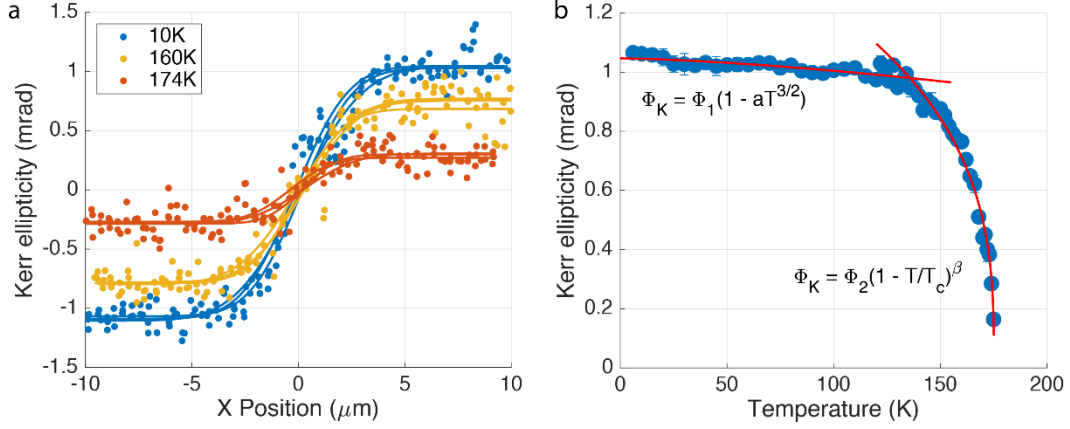


Figure S1 | **a** dc Kerr ellipticity plotted as a function of position relative to the center of the domain wall for various temperatures. The ellipticity data (dots) are subsequently fit to error functions (lines). **b** The temperature dependence of dc Kerr ellipticity compared to predictions for the spin wave (low temperature) and critical (high temperature) regimes, respectively.

II. Analysis of domain wall width and displacement

Domain wall (DW) width and displacement were characterized by measuring both Φ_{dc} and the ac modulation synchronous with the applied magnetic field, $\delta\Phi_{ac}$, as a function of position along a direction normal to the DW. There are three length scales associated with this measurement: DW displacement, Δx , DW width, w , and laser focus radius, σ .

Scanning the laser probe transverse to the domain wall yields a peak in $\delta\Phi_{ac}/\Phi_{dc}$ as a function of position, as discussed in the main text. With knowledge of σ by standard methods, we can obtain Δx and, in certain regimes, w , from the height and width of this peak.

Regime I: w small compared to the laser spot.

For $w < \sigma$, the height of the peak is given by

$$(\delta\Phi_{ac}/\Phi_{dc})_{DW} = \text{erf}(\Delta x/\sqrt{2}\sigma), \quad (2)$$

and its width is given by σ . Both peak amplitude and width are independent of w .

Regime II: w comparable or larger than the laser spot radius.

Eq. 2 is modified if the wall width is comparable to the laser spot radius. In this case the width of the peak broadens to $\sigma_{\text{total}}^2 = \sigma^2 + w^2$ and the peak amplitude is given approximately by

$$(\delta\Phi_{ac}/\Phi_{dc})_{DW} = \text{erf}(\Delta x/\sqrt{2}\sigma_{\text{total}}). \quad (3)$$

III. Domain wall width

Below approximately 160 K the width of the peaks observed in scans across the DWs are resolution limited. However, above 160 K the peak is broadened, suggesting that w has become comparable to σ . This observation is consistent with the analysis of Bulaevskii and Ginzburg, who predicted that w is equal to the correlation length¹ and diverges at the critical temperature,

$$w(T) \propto \left(1 - \frac{T}{T_c}\right)^{-\beta}. \quad (4)$$

Figs. S2(a)-(e) show maps of $\delta\Phi_{ac}/\Phi_{dc}$ measured at temperatures ranging from 150 K to 168 K. The width of the wall was estimated from Gaussian fits to the Kerr signal measured along the white dashed lines indicated in the maps. The full-width half maximum values are plotted in Fig. S2(f) and show that the wall broadens beyond the resolution limit as T_c is approached.

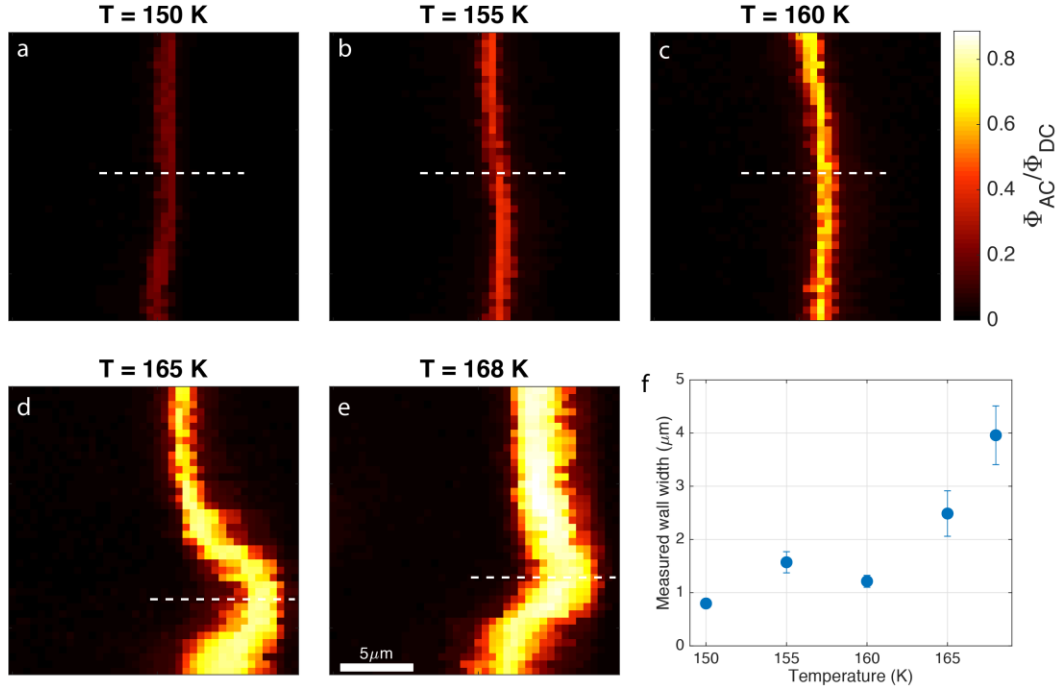


Figure S2 | **a-e** Temperature dependence of the ac Kerr ellipticity maps. The amplitude of the magnetic field was 27 Oe and the frequency was 1 kHz. **f** The domain wall widths estimated from the Gaussian fits are plotted against temperature. Note that the instrument resolution (1 μm) sets the upper bound of the wall width estimations. The error bars indicate the uncertainties of the least-square fitting of the data.

In principle the width of the peaks in $\delta\Phi_{ac}/\Phi_{ac}$ vs. position could also broaden if the displacement itself is larger than the optical resolution. However, in this case the width should depend on the amplitude of the magnetic field that drives the wall motion. To pin down the source of the broadening at high temperature, maps (Figs. S3a-d) were measured under various magnetic field strengths at $T = 165$ K. The maps and the estimated wall widths (Fig. S3e) indicate that w is independent of the amplitude of the ac magnetic field. Thus the observed broadening near the critical temperature arises from the diverging wall width and not because the DW displacement becomes larger than the resolution.

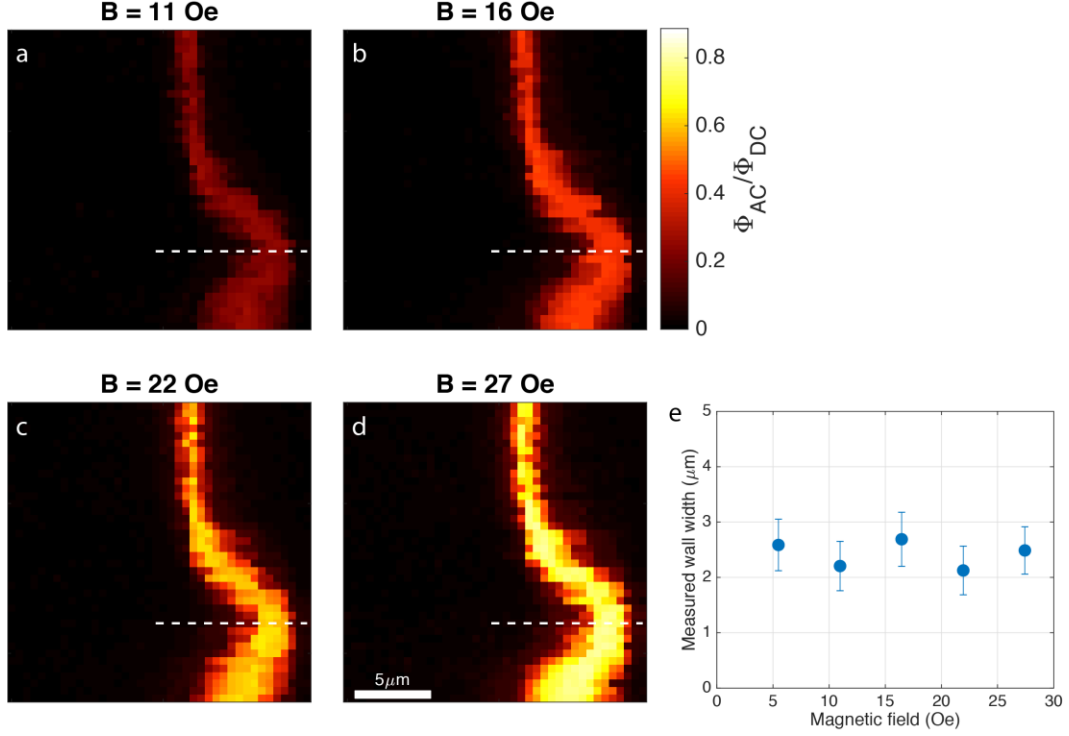


Figure S3 | a-e Maps of ac Kerr ellipticity maps at $T = 165\text{ K}$ and $f = 1\text{ kHz}$ at the indicated magnetic fields. e Domain wall width plotted as a function of magnetic field. The error bars indicate the uncertainties of the least-square fitting of the data.

IV. Estimation of domain wall mobility

The DW mobility, μ , relates the wall velocity, v , to the applied magnetic field, H . In our measurements the velocity is a nonlinear function of the field, with little or no wall motion below a threshold field, H_{th} . Below we test if the nonlinear velocity-field relation can be described by the scaling relation,

$$\frac{dx}{dt} = \mu H_{th} f\left(\frac{H}{H_{th}}\right), \quad (5)$$

Where x is the wall position, $f(z)$ is a scaling function, and μ is a coefficient with dimensions of mobility. From Eq. 5, the domain wall displacement Δx induced by $H(t) = H \sin \omega t$ is given by,

$$\Delta x = \mu H_{th} \int_0^{\pi/2\omega} dt f(H \sin \omega t / H_{th}) \quad (6)$$

With definition $\rho \equiv H/H_{th}$ and change of variables $y = \rho \sin \omega t$ we have,

$$\Delta x = \mu H_{th} \int_0^\rho \frac{dy f(y)}{\omega \rho \cos(\sin^{-1} y/\rho)} = \frac{\mu H_{th}}{\omega \rho} \int_0^\rho \frac{dy f(y)}{\sqrt{1 - y^2/\rho^2}} \quad (7)$$

and

$$\frac{\omega \Delta x}{H_{th}} = \frac{1}{\rho} \int_0^\rho \frac{dy f(y)}{\sqrt{1 - y^2/\rho^2}} = F(\rho) = F\left(\frac{H}{H_{th}}\right). \quad (8)$$

Thus the prediction of the ansatz expressed by Eq. 5 is that curves of displacement vs. magnetic field measured at different frequencies should collapse to single curve, $F(\rho)$, when $\omega \Delta x / H_{th}$ is plotted vs. H / H_{th} . This is the data collapse shown in Fig. 3(d) of the main text.

The linearity of the scaling function $F(\rho)$ above threshold motivated testing a simple model for the nonlinear mobility, namely that that differential mobility dv/dH is zero below threshold and constant above. With reference to Eq. 5, this associates the parameter μ with the differential mobility above threshold and sets $f(y) = 0$ for $\rho < 1$ and $f(y) = y - 1$ for $\rho > 1$. In this case Eq. 9 becomes,

$$\frac{\omega \Delta x}{H_{th}} = \frac{1}{\rho} \int_1^\rho \frac{(y - 1) dy}{\sqrt{1 - y^2/\rho^2}}, \quad (9)$$

which is the dashed line in Fig. 3(d). As discussed in the main text, we use this scaling procedure to obtain the differential mobility as a function of temperature.

V. Spatial variation of the domain wall mobility

The ac Kerr ellipticity exhibits a certain amount of spatial variation. Depending on the specific location of the measurement spot (Fig. S4a), the DW mobility can vary by a factor of two, while the threshold field H_{th} exhibits a much smaller variation (Fig. S4b-g). However, the non-monotonic temperature dependence of the DW mobility is observed for all DWs, as shown in the ac maps plotted in Fig. 2 of the main text.

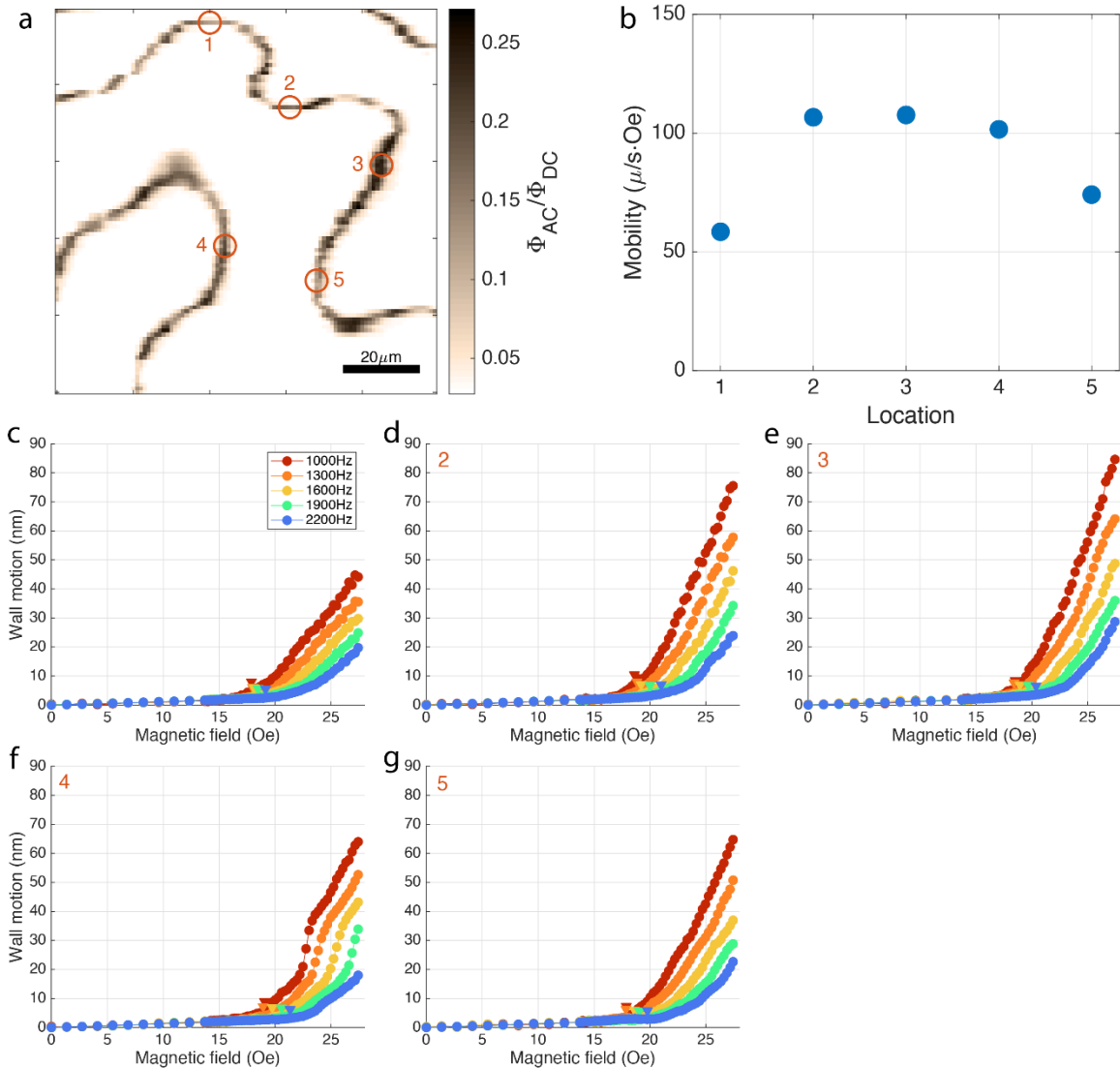


Figure S4 | **a** ac MOKE map measured at 130 K. **b** Plot of DW mobility at the five different locations indicated panel **a**. **c-g**. Plots of the temperature dependent AC Kerr response at these five locations, showing variations in DW mobility.

VI. Temperature dependence of domain wall mobility

The DW mobility results plotted in Fig. 3(e) are fitted using the expression derived by Garanin, covering the full temperature range across the phase transition from elliptical to linear domain walls¹:

$$\mu(T) = \begin{cases} -\mu_1 \left[\frac{2}{3} - \left(1 - \frac{T}{T_{BG}}\right)^{-\beta_1} + \frac{1}{3} \left(1 - \frac{T}{T_{BG}}\right)^{-2\beta_1} \right]^{-1}, & T < T_{BG} \\ \frac{2}{3} \mu_2 (1 - T_c)^{-2\beta_2}, & T \geq T_{BG} \end{cases}, \quad (10)$$

where β_1 and β_2 are the critical exponents of order parameters M_x and M_z , respectively. We obtain $\beta_1 = 0.31 \pm 0.20$ and $\beta_2 = 1.15 \pm 0.41$.

VII. Nucleation temperature vs. rate of heating

Below we obtain an expression for the probability of nucleation vs. rate of heating for a model in which nucleation occurs by thermal excitation over a barrier. In such a model we have,

$$\frac{dP(t)}{dt} = -P(t)v_0 \exp\left(-\frac{E_b}{k_B T}\right), \quad (11)$$

where P , v_0 , and E_b are the occupancy of the initial metastable state, the escape attempt rate, and the barrier height, respectively. For a constant heating rate, $R \equiv dT/dt$,

$$\frac{dP(t)}{dT} = -\frac{P(t)v_0}{R} \exp\left(-\frac{E_b}{k_B T}\right). \quad (12)$$

The integral of this equation,

$$\int_1^P \frac{dP'}{P'} = -\frac{v_0}{R} \int_{-\infty}^T \exp\left(-\frac{E_b}{k_B T'}\right) dT', \quad (13)$$

yields the probability of occupancy as a function of temperature and heating rate,

$$P(T, R) = \exp\left\{-\frac{v_0}{R} \left[T \exp\left(-\frac{E}{k_B T}\right) - \frac{E}{k_B} \Gamma_0\left(\frac{E}{k_B T}\right)\right]\right\}, \quad (14)$$

where $\Gamma_0(z)$ is the gamma function. For large values of $E/k_B T$ the above expression simplifies to,

$$P(T, R) \approx \exp\left\{-\frac{v_0}{R} \left[\frac{k_B T^2}{E} \exp\left(-\frac{E}{k_B T}\right)\right]\right\}. \quad (15)$$

Fig. S5 shows a plot of $P(T, R)$ for several heating rates in the range from 1-100 mK/s. The attempt rate $v_0 = 10^{10} s^{-1}$ and $E/k_B = 3000K$ are chosen so that the nucleation temperature is near 130 K, as observed in the experiment. The plot shows that the predicted nucleation temperature shifts approximately 10 K for each decadal change in heating rate. This shift is independent of the choice of R and v_0 , as long as they are chosen such that the nucleation takes place near 130 K.

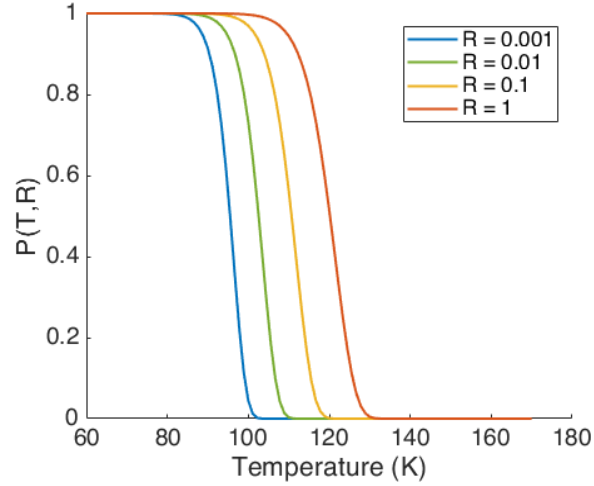


Figure S5 | Plot of the probability of occupancy $P(T, R)$ as a function of temperature, for selected values of heating rates ranging from 1 to 1000 mK/s.

We tested the model of thermal activation over a barrier by performing measurements of the nucleation temperature T_n vs. heating rate in the range from 0.1K/min to 1K/min. Similar to the measurements shown in Fig. 4 of the main text, a single domain sample, prepared by cooling in a field, was warmed at a constant heating rate under zero magnetic field. As shown in Fig. S5, T_n was found to shift by no more than 200 mK when the heating rate was increased by a factor of ten, strongly indicating that nucleation does not result from thermal activation over a barrier. This result led to us to consider a model (described in the following section) in which the energy barrier to nucleate a pair of domain walls goes to zero with increasing temperature.

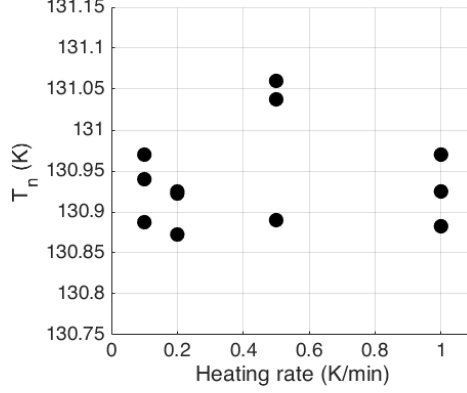


Figure S5 | Nucleation temperature as a function of heating rate. A fully magnetized sample was warmed at various heating rates under zero magnetic field. The nucleation temperature T_n is shown to be independent of the heating rate.

VIII. Nucleation energy for domain walls

We use a simple model to estimate the energy required to nucleate a pair of linear domain walls.

The free energy density (per unit area) of a static magnetic texture $M_z(x)$ is given by,

$$F = \int dx \left[\rho_s \left(\frac{dM_z}{dx} \right)^2 + \frac{1}{4\chi_{\parallel}} (M_z^2 - M_s^2)^2 - M_z H \right], \quad (16)$$

where ρ_s is the spin stiffness parameter, χ_{\parallel} is the longitudinal susceptibility, and M_s is the saturated magnetization². Rewriting in terms of the normalized magnetization, $m \equiv M_z/M_s$, we have,

$$\frac{F}{M_s^2} = \int dx \left[\rho_s \left(\frac{dm}{dx} \right)^2 + \frac{1}{4\chi_{\parallel}} (m^2 - 1)^2 - \frac{mH}{M_s} \right]. \quad (17)$$

For the case of zero external field, we take $H = -M_s$, which is the demagnetization field in a slab geometry. Then we have,

$$\frac{F}{M_s^2} = \int dx \left[\rho_s \left(\frac{dm}{dx} \right)^2 + \frac{1}{4\chi_{\parallel}} (m^2 - 1)^2 + m \right] \quad (18)$$

We can write this expression in the form,

$$\frac{F}{M_s^2} = \rho_s \int dx \left[\left(\frac{dm}{dx} \right)^2 + \frac{1}{4\xi^2} (m^2 - 1)^2 \right] + \int dx m, \quad (19)$$

where ξ is the correlation length and we have used the relation, $\rho_s \chi_{\parallel} = \xi^2$.

Next, we specify that the magnetization texture corresponds to pair of linear domain walls with width w and separation s such that³,

$$m(x, s, w) = 1 - \left[\tanh\left(\frac{x+s}{w}\right) + \tanh\left(\frac{-x+s}{w}\right) \right]. \quad (20)$$

This expression for the magnetization profile is then substituted into Eq. 19 to obtain the free energy as function of wall separation for different values of χ_{\parallel} that is shown in Fig. 4(e) of the main text. We follow Bulaevskii and Ginzburg⁴ in equating the correlation length with the DW width, i.e. $\xi = w$.

IX. Dependence of nucleation temperature on external magnetic field

Based on the model described above, we derive an approximate expression for the dependence of the nucleation temperature on the applied field. As discussed above, abrupt nucleation occurs when the barrier goes to zero. As shown in Fig. 4(d), zero barrier occurs when the free energy density at wall separation $s \approx w$ is equal to the free energy density for $s = 0$. The value of F/M_s^2 for the single domain slab ($s = 0$) is simply equal to the length of the slab L .

Now, we rewrite Eq. 15 as the sum of two terms, where only the second term depends on the external field,

$$\frac{F(s = w)}{M_s^2} = F_1[m(x, s = w)] + F_2[m(x, s = w), H_{ext}]. \quad (21)$$

The second (Zeeman) term is given by,

$$F_2[m(x, s = w), H_{ext}] = L - 4(1 + h)w, \quad (22)$$

where $h \equiv H_{ex}/M_s$. The condition for nucleation is that,

$$F_1[m(x, s = w)] + L - 4(1 + h)w = L, \quad (23)$$

or

$$F_1[m(x, s = w)] = 4(1 + h)w. \quad (24)$$

We calculate the rate of change of the nucleation temperature with applied field by taking the derivative of both sides with respect to T ,

$$\frac{d}{dT} F_1[m(x, s = w)] = 4w \frac{dh}{dT}. \quad (25)$$

In the limit that the applied field and temperature shift are small, we can approximate F_1 by its value in zero field, which is $4w$, leading to,

$$\frac{dh}{dT} = \frac{d}{dT} \ln F_1. \quad (26)$$

As F_1 is inversely proportional to the longitudinal susceptibility, χ_{\parallel} , we obtain Eq. 5 of the main text,

$$\frac{dT_n}{dH} = \frac{1}{M_s \left[\frac{d}{dT} \ln\{\chi(T)\} \right]_{T=T_n}}, \quad (27)$$

where we have restored $H = hM_s$,

References

- 1 Garanin, D. A. Dynamics of elliptic domain walls. *Physica A: Statistical Mechanics and its Applications* **178**, 467-492, doi:10.1016/0378-4371(91)90033-9 (1991).
- 2 Hartl-Malang, M., Kotzler, J. & Garanin, D. A. Domain-wall relaxation near the disorder transition of Bloch walls in Sr hexaferrite. *Phys Rev B Condens Matter* **51**, 8974-8983, doi:10.1103/physrevb.51.8974 (1995).
- 3 Loxley, P. N. Rate of magnetization reversal due to nucleation of soliton-antisoliton pairs at point-like defects. *Physical Review B* **77**, doi:10.1103/PhysRevB.77.144424 (2008).
- 4 Bulaevskii, L. N. & Ginzburg, V. L. Temperature Dependence of the Shape of the Domain Wall in Ferromagnetics and Ferroelectrics. *Sov. Phys. JETP* **18** (1964).